

## ORIGINAL ARTICLE

# Multifunctional interleaved geometric-phase dielectric metasurfaces

Elhanan Maguid<sup>1</sup>, Igor Yulevich<sup>1</sup>, Michael Yannai<sup>1</sup>, Vladimir Kleiner<sup>1</sup>, Mark L Brongersma<sup>2</sup> and Erez Hasman<sup>1</sup>

Shared-aperture technology for multifunctional planar systems, performing several simultaneous tasks, was first introduced in the field of radar antennas. In photonics, effective control of the electromagnetic response can be achieved by a geometric-phase mechanism implemented within a metasurface, enabling spin-controlled phase modulation. The synthesis of the shared-aperture and geometric-phase concepts facilitates the generation of multifunctional metasurfaces. Here shared-aperture geometric-phase metasurfaces were realized via the interleaving of sparse antenna sub-arrays, forming Si-based devices consisting of multiplexed geometric-phase profiles. We study the performance limitations of interleaved nanoantenna arrays by means of a Wigner phase-space distribution to establish the ultimate information capacity of a metasurface-based photonic system. Within these limitations, we present multifunctional spin-dependent dielectric metasurfaces, and demonstrate multiple-beam technology for optical rotation sensing. We also demonstrate the possibility of achieving complete real-time control and measurement of the fundamental, intrinsic properties of light, including frequency, polarization and orbital angular momentum.

*Light: Science & Applications* (2017) 6, e17027; doi:10.1038/lsa.2017.27; published online 11 August 2017

**Keywords:** geometric phase; metasurface; multifunctional; shared aperture; spectropolarimetry; spin-optics; Wigner distribution

## INTRODUCTION

Multitasking shared-aperture systems have initially emerged as phased array radar antennas<sup>1–3</sup>. Recently, the shared-aperture concept has been suggested as a platform for multifunctional optical phased array antennas, accomplished by a reflective metasurface<sup>4</sup>. Metasurfaces consist of metallic or dielectric subwavelength nanoantennas, capable of manipulating light by controlling the local amplitude and phase of an incident electromagnetic wave<sup>5–17</sup>. Shared-aperture interleaved phased arrays are formed by the random interspersing of sub-arrays, thus resulting in a device with high flexibility in multifunctional wavefront generation and the angular resolution of the shared aperture. Each sub-array is associated with a specific phase function, sparsely sampled at randomly chosen lattice points. The random sampling as well as the antennas' size affect the dominant mechanism responsible for creating an undesired background noise—for sub-wavelength nanoantennas, speckle noise appears, whereas for larger antennas, most of the noise is attributed to sidelobes<sup>2,4</sup>. The noise imposes a fundamental limitation to the system's information capacity. Therefore, knowledge of such limitations can guide the design of optimal devices based on multifunctional metasurface. Here the interleaved geometric-phase metasurface (GPM) served as a platform to study those limitations.

The shared-aperture GPM is obtained by the incorporation of the geometric-phase mechanism into interleaved structures, which enables spin-control capabilities. GPMs are composed of anisotropic

nanoantennas that generate a local phase delay, corresponding to an orientation function  $\phi_g(x, y) = 2\sigma\theta(x, y)$ <sup>6,7,12,18,19</sup>. Here  $\theta(x, y)$  is the in-plane nanoantenna orientation and  $\sigma = \pm 1$  denotes the polarization helicity, that is, right ( $\sigma_+$ ) or left ( $\sigma_-$ ) circular polarization, respectively. Due to the interaction with the nanoantennas of varying orientations, the light's polarization state attained at different points traverses various paths on the Poincaré sphere. This results in a Pancharatnam–Berry phase pick-up between any pair of nanoantennas, which is equal to half the area of the corresponding geodesic triangle  $\Omega$  on the Poincaré sphere<sup>7,18</sup> (Figure 1b).

## MATERIALS AND METHODS

### Fabrication of Si-GPM

The poly-Si thin film with a thickness of 260 nm was grown at a temperature of 600 °C on a SiO<sub>2</sub> (fused silica) substrate. The photoresist CSAR 6200.09 (Allresist GmbH, Strausberg, Germany) with a thickness of 190 nm was deposited on the poly-Si film and baked at 150 °C for 1 min. For the pattern transfer onto the poly-Si film, the photoresist mask was made using Raith e-LiNE E-beam lithography system (Raith, Dortmund, Germany), then baked at 130 °C for 1 min and etched using deep reactive-ion etching by F-ICP Plasma Therm system (Plasma-therm, Saint Petersburg, FL, USA) for 30 s.

<sup>1</sup>Micro and Nanooptics Laboratory, Faculty of Mechanical Engineering, and Russell Berrie Nanotechnology Institute, Technion—Israel Institute of Technology, Haifa 32000, Israel and <sup>2</sup>Geballe Laboratory for Advanced Materials, Stanford University, 476 Lomita Mall, Stanford, CA 94305, USA

Correspondence: E Hasman, Email: mehasman@technion.ac.il

Received 26 October 2016; revised 16 February 2017; accepted 23 February 2017; accepted article preview online 24 February 2017

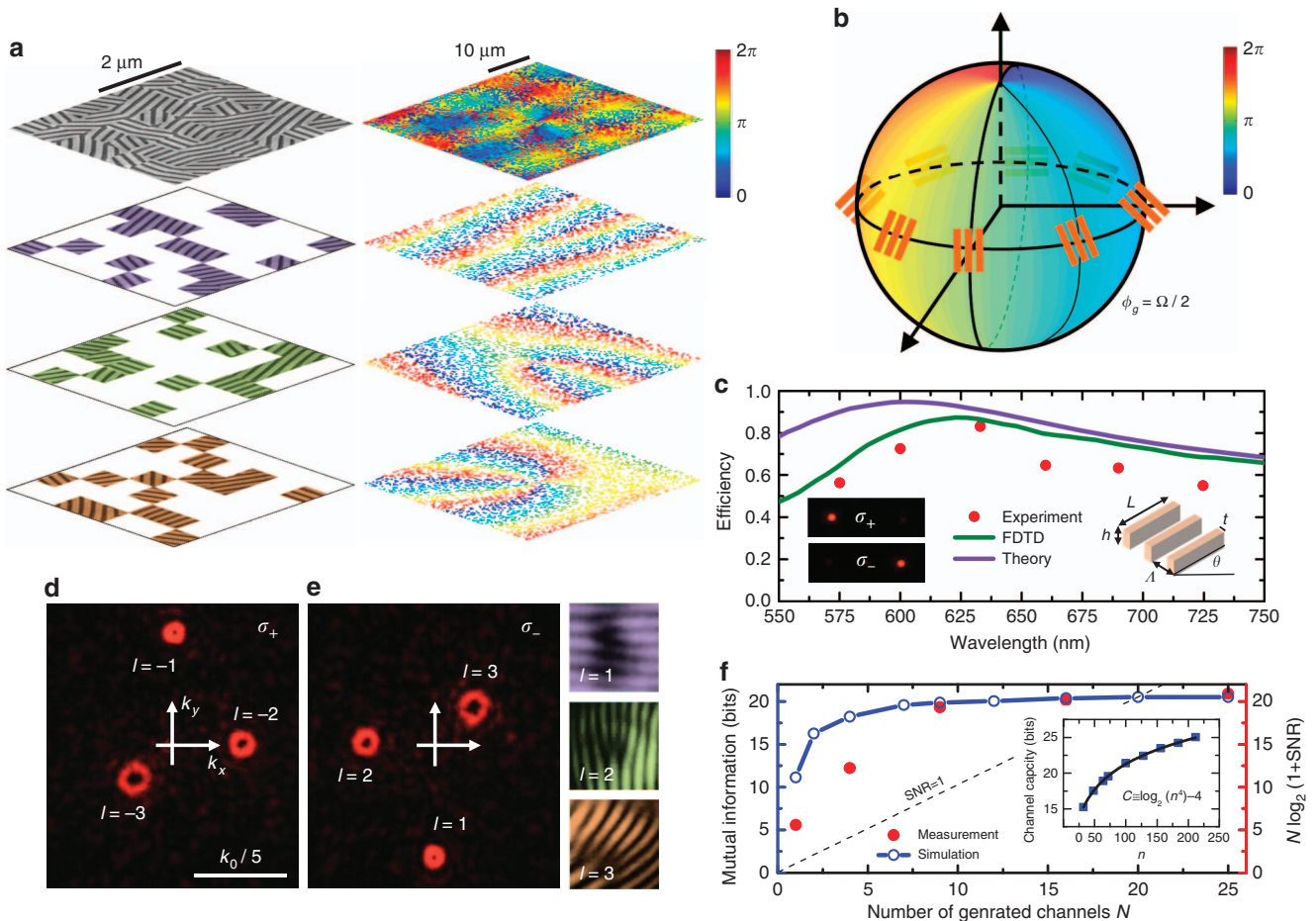


**Figure 1** Interleaved GPM concept. (a) Sparse geometric-phase profiles and the resultant interleaved phase (right panel). Left panel depicts the corresponding SEM images of the interleaved GPM. (b) Illustration of the geometric phase pick-up principle via the Poincaré sphere. The phase pick-up  $\phi_g$  is equal to half the area of the geodesic triangle  $\Omega$ . (c) Measured diffraction efficiency at various wavelengths for a linear phase GPM (red circles), and the corresponding FDTD simulation (green) and effective medium theory calculation (purple). Right inset illustrates the designed Si-BB oriented at an angle  $\theta$ , where  $h=260$  nm,  $L=600$  nm,  $t=70$  nm and  $\Lambda=200$  nm. Left inset depicts the measured far-field intensity distributions of the linear phase GPM for  $\sigma_+$  and  $\sigma_-$  illumination at a wavelength of 630 nm. (d, e) Measured spin-flip momentum deviation of different optical angular momentum wavefronts, where  $\sigma$  denotes the incident spin and  $k_0$  is the incident wave number. Insets show the interference patterns of a plane-wave with the vortex beams for  $\sigma_-$  and  $l=1,2,3$ , verifying the desired topological charges. (f) Calculated mutual information (blue line, left axis) and measured total number of bits (red dots, right axis) for a varying number of channels ( $M$ ); dashed black line depicts the distinguishability limit for the generated channels. Inset shows the calculated relation between the number of nanoantennas in each of the lattice's dimensions ( $n$ ) and the channel capacity ( $C$ ). FDTD, finite-difference time-domain; SNR, signal-to-noise ratio.

### Metasurface design parameters

Figure 2 shows the scanning electron microscopy (SEM) image of a resultant interleaved GPM with the designed Si-building blocks (BBs). Each Si-BB is composed of several nanorods, where their number is determined according to the orientation angle  $\theta$  so as to fill an area of  $600 \times 600$  nm<sup>2</sup>. The nanorods are of 70 nm width and 260 nm depth, arranged 200 nm apart from each other (center to center, see also Figure 1e). The metasurface diameter was of 50  $\mu$ m. These parameters were maintained for all the fabricated metasurfaces.

### Experimental set-up

Figure 3 depicts the experimental set-up used in all of our measurements. The input beam, generated by a supercontinuum laser source (Fianium Supercontinuum SC450, Fianium, Southampton, UK) was temporally modulated by an acousto-optic modulator (Fianium AOTF V1, Fianium, Southampton, UK) facilitating the use of multi-wavelength laser light. The beam

was then spatially filtered and collimated. A non-polarizing beam splitter followed by a reflection mode phase only spatial light modulator (Hamamatsu PPM X8267, Hamamatsu, Shizuoka Pref. Hamamatsu City, Japan) were used in order to generate the helical phase profiles needed for the optical angular momentum (OAM) spectropolarimeter metasurface (OSPM) experiments (Figure 6). The beam's polarization state was set using a polarization generator (linear polarizer followed by a quarter wave plate), and the beam was subsequently focused on the sample. The diffracted light was collected using an objective lens (Olympus SLMPlan 50  $\times$  0.45, Olympus Corporation, Shinjuku, Tokyo, Japan) and the obtained magnified image was then Fourier transformed using a second lens. The output beam's polarization state was analyzed using a polarizer-analyzer (Figure 3a) or two linear polarizers placed parallel and set at a relative angle of 45° (Figure 3b; for the OSPM experiments). The obtained images were taken using a RGB CMOS camera (Ximea MQ022CG-CM, Ximea Corp. Münster, Germany).

### Stokes parameters

In order to determine the Stokes parameters, the detected pattern upon a CMOS camera should be provided with the intensities  $I_{\sigma_-}$ ,  $I_{\sigma_+}$  and  $I_{L45}$ ,  $I_{L0}$ . The spin-dependent beams determine the intensities  $I_{\sigma_{\pm}}$ , whereas the spin-independent beams, projected on a linear polarizer, determine the linearly polarized intensities  $I_{L0}$  and  $I_{L45}$ , respectively. The Stokes parameters are then calculated by the following expressions:  $S_0 = 2(I_{\sigma_+} + I_{\sigma_-})/\eta$ ;  $S_3 = 2(I_{\sigma_+} - I_{\sigma_-})/\eta$ ; and  $S_1 = 2I_{L0}/\eta - S_0$ ;  $S_2 = 2I_{L45}/\eta - S_0$ , where  $\eta$  is determined by a calibration experiment<sup>20</sup>.

### RESULTS AND DISCUSSION

We designed an efficient dielectric GPM, using a Si-based BB, constructed of several nanorods that operate as an anisotropic  $\pi$  retarder. The BBs were arranged in a square array with a lattice constant of 600 nm (see Materials and Methods). The realized GPM provides a maximal diffraction efficiency of  $\sim 85\%$ , which was measured for the transmission mode of a single channel, in agreement with an effective medium theory calculation and FDTD simulation (Figure 1c). Note, the imaginary part of the refractive index of the Si was taken into account by the FDTD calculations<sup>12</sup>.

In order to demonstrate the interleaving concept, we designed a shared-aperture Si-GPM (Figure 1a) generating multiple off-axis

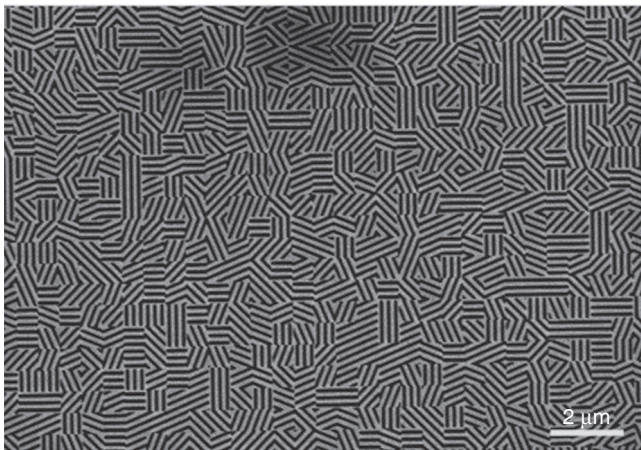


**Figure 2** SEM image of the interleaved Si-based GPM.

wavefronts carrying OAM (scalar vortices). Therefore, the BB's orientation was arranged according to the relation  $2\theta_j(x, y) = (\mathbf{k} \cdot \mathbf{r} + l\varphi)_j$ , to obtain a linear momentum redirection of  $\sigma\mathbf{k}_j$  and scalar vortices of topological charge  $\sigma l_j$ , where  $\varphi$  is the azimuthal angle and  $\mathbf{r}_j = (x, y)_j$  is the position of each BB at the  $j$ th sub-array. We observed spin-dependent OAM carrying wavefronts with the desired topological charges of  $\pm 1$ ,  $\pm 2$  and  $\pm 3$  at a wavelength of 630 nm (Figure 1d and 1e). Moreover, diffraction-limited spot-sizes corresponding to the GPM's full aperture were confirmed (Supplementary Figs. S1 and S2).

The limitation of the number of modes (channels) that can be generated by an interleaved GPM is analyzed in terms of information capacity by means of the Wigner position-momentum  $(\mathbf{x}, \mathbf{k})$  distribution in phase-space<sup>21</sup>. The spin-dependent Wigner function of a shared-aperture GPM is represented by  $W_{\sigma}^{(N)}(\mathbf{x}, \mathbf{k}) = \int \psi_{\sigma}^{(N)}(\mathbf{x} + \xi) \left\{ \psi_{\sigma}^{(N)}(\mathbf{x} - \xi) \right\}^* \exp(2i\xi \cdot \mathbf{k}) d\xi$ , where  $\psi_{\sigma}^{(N)}(\mathbf{x}) = \exp(-i\phi_{\sigma}^{(N)}(\mathbf{x}))$  is the phase function corresponding to  $N$  interleaved channels for  $\sigma = \pm 1$  illumination. We estimate the GPM's channel capacity ( $C$ ), that is, the number of distinct channels that can be opened, utilizing the spin-dependent mutual information (MI),  $MI_{\sigma}^{(N)} = \int W_{\sigma}^{(N)}(\mathbf{x}, \mathbf{k}) \log_2 \left\{ W_{\sigma}^{(N)}(\mathbf{x}, \mathbf{k}) / [\rho_{\sigma}^{(N)}(\mathbf{x}) \pi_{\sigma}^{(N)}(\mathbf{k})] \right\} d\mathbf{k} d\mathbf{x}$ , where  $\rho_{\sigma}^{(N)}(\mathbf{x}) = \int W_{\sigma}^{(N)}(\mathbf{x}, \mathbf{k}) d\mathbf{k}$  and  $\pi_{\sigma}^{(N)}(\mathbf{k}) = \int W_{\sigma}^{(N)}(\mathbf{x}, \mathbf{k}) d\mathbf{x}$  are the marginal density functions in position and momentum space (Supplementary Fig. S3), respectively<sup>22,23</sup>. Figure 1f depicts the numerically calculated MI for an interleaved GPM size of  $40 \times 40 \mu\text{m}^2$ , where the total number  $n \times n$  of nanoantennas is  $80 \times 80$ . The number of bits of information carried by all channels  $N \log_2(1 + \text{SNR})$  was obtained via measurements of the signal-to-noise ratio (SNR) for each channel as a function of the number of channels,  $N$  (Figure 1f; Supplementary Fig. S1). These results are in agreement with the relation  $MI \approx N \log_2(1 + \text{SNR})$  as predicted by information theory<sup>24</sup>. The GPM's channel capacity is bounded by the external condition where each channel is allocated with a single bit (SNR = 1). Thus, a value of  $C \approx 20$  can be estimated from Figure 1f, as well as from the relation  $C = \sup\{MI\}$ . Our simulations show that the channel capacity is also affected by the total number of nanoantennas and was found to increase according to  $C \approx \log_2(n^4) - 4$  (Figure 1f, inset), wherein the fourth power evidently equals the phase-space dimensionality. Note, the intensity per channel decreases according to  $1/N^2$ , as a result of speckle noise<sup>4</sup> (Supplementary Fig. S1). The introduced

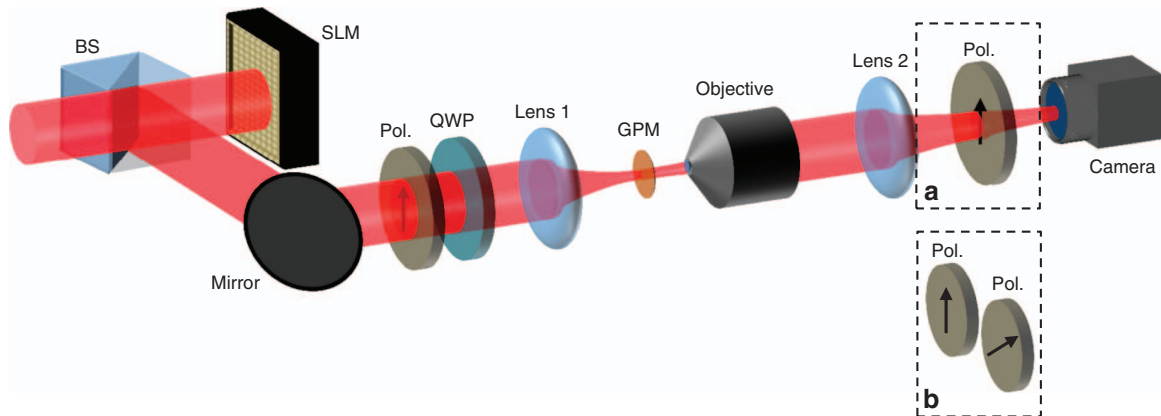


**Figure 3** Experimental set-up. (a) A single polarizer used in the optical rotatory dispersion and spectropolarimetry experiments. (b) Two linear polarizers placed parallel and set at a relative angle of  $45^\circ$  for the optical angular momentum spectropolarimeter metasurface experiments. The focal lengths for the two lenses are 80 and 50 mm, respectively. BS, beam splitter; Pol., polarizer; QWP, quarter wave plate; SLM, spatial light modulator.

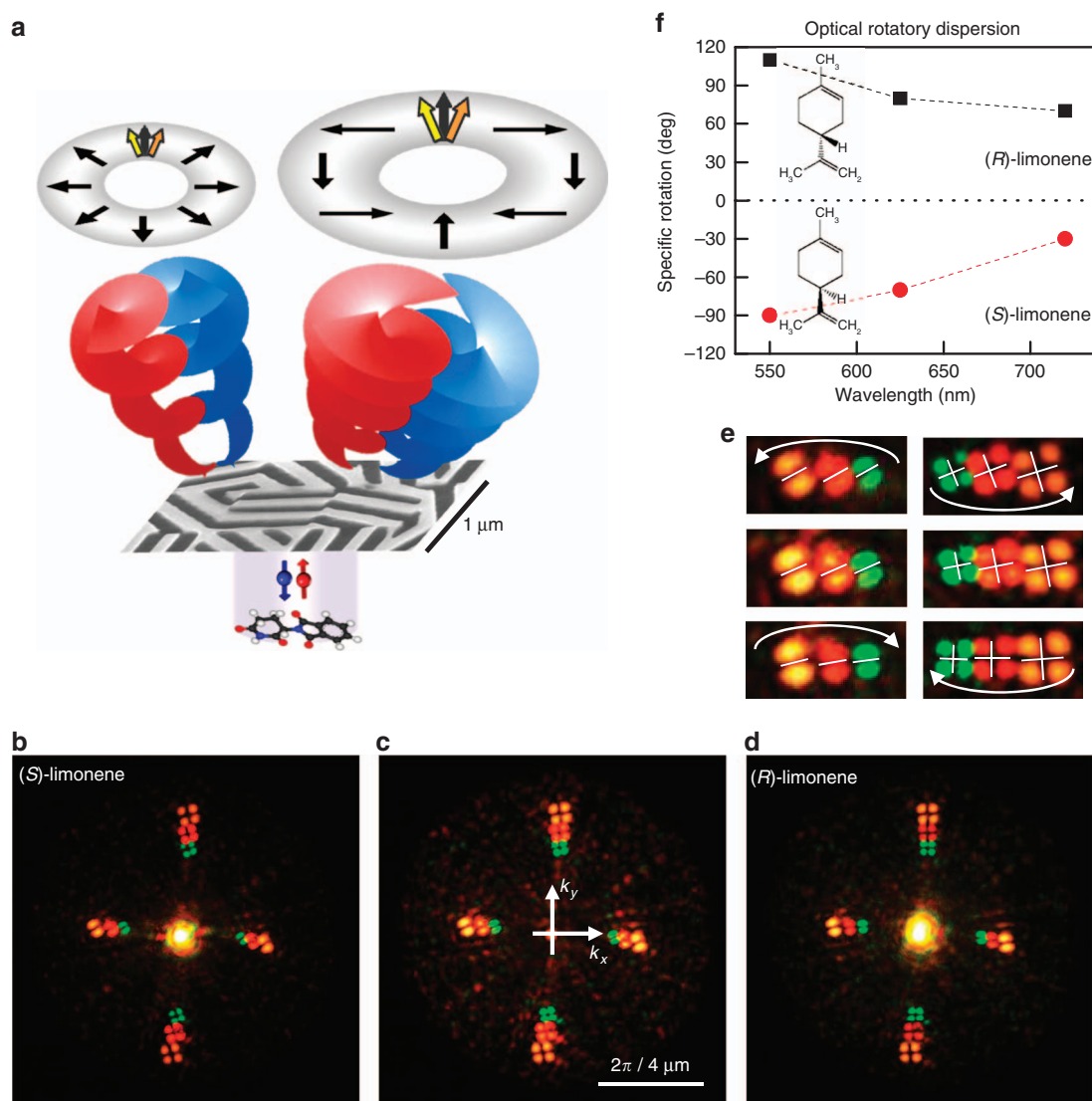


**Figure 4** ORD measurement by interleaved GPM. **(a)** Schematic of vectorial vortex beams with winding numbers  $l=1$  and  $l=2$  emerging from a GPM (SEM image) illuminated with linearly polarized light; red and blue helices represent scalar vortices of opposite helicities and OAMs. **(b–d)** Observed diffraction patterns of interleaved vectorial vortices generated by using linearly polarized light passing through (S)-limonene **(b)**, air **(c)** and (R)-limonene **(d)** at wavelengths of 550, 630 and 725 nm, with a fixed angle polarizer–analyzer. **(e)** Enlarged spots (corresponding to **b–d**, top down) illustrating the wavelength-dependent rotation of the vectorial vortices for (S)- and (R)-limonene. **(f)** ORD measurements of (S)- and (R)-limonene, represented by red circles and black squares, respectively. Insets show the corresponding chemical structure. ORD, optical rotatory dispersion.

information capacity analysis enables to choose a certain shared-aperture metasurface dimension and amount of nanoantennas to achieve a high SNR in demultiplexing light in different frequencies, polarization states and OAM by packing several functions into a single area. For a metasurface demultiplexing four channels and 5 bits dynamic range imaging system, we estimated the GPM parameters to be  $n \approx 80$ , and  $D \approx 50 \mu\text{m}$  for 600 nm size of BB, providing the required 20 bits of information capacity (Figure 1f, inset). Consequently, we implemented GPMs with such parameters that operate within the fundamental limits.

GPMs enable space-variant polarization manipulation, producing a broad class of wavefronts such as vectorial vortices. This class of complex beams, signatred with a polarization singularity, is of special interest for optical fiber communication systems, optical

tweezers, tractor beams and laser beam shaping<sup>25,26</sup>. Interleaved GPMs facilitate the generation of multiple vectorial vortices by coherent superposition of multiplexed scalar vortices with opposite helicities (Figure 4a). This superposition is attained by illuminating the GPM with linearly polarized light. The resultant beams are characterized by axially symmetric polarization states. Therefore, projecting these vectorial vortices on a linear polarizer reveals a petal-shaped diffraction pattern. A change in the incident linear polarization angle is manifested by a constant phase difference between the right and left circular polarizations. Hence, the fringes of the pattern rotate when the input linear polarization angle is altered. This phenomenon can be utilized to measure the specific rotation of a chiral molecule, which enables, for example, the distinction between two enantiomers at a certain wavelength. Moreover,

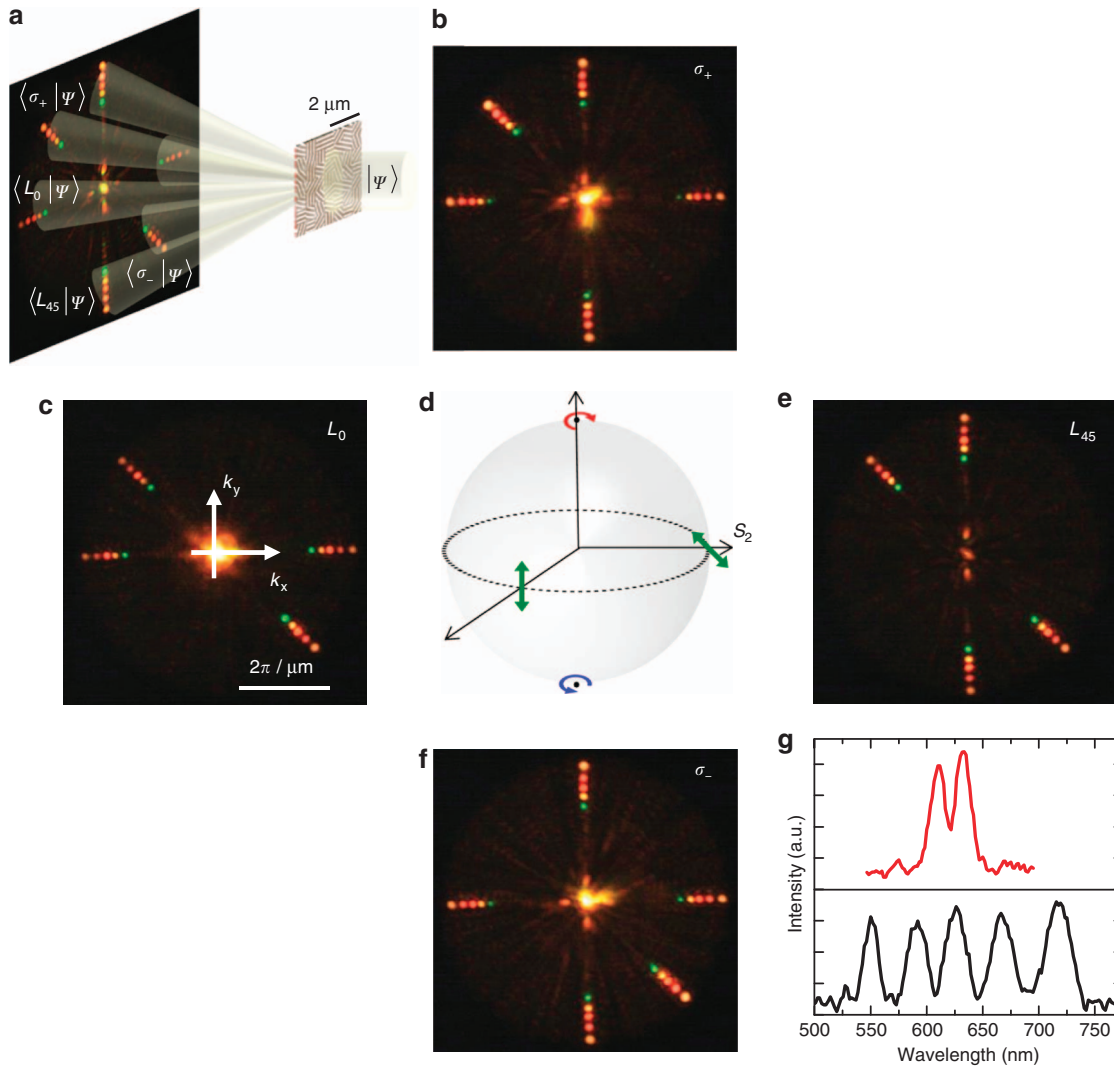


**Figure 5** Si-based SPM. (a) Schematic set-up of the SPM illuminated by an elliptically polarized polychromatic light source; the projection on different polarization components is then captured by a charge-coupled device camera. (b–f) Measured far-field intensities for different input polarizations:  $\sigma_+$  (b),  $\sigma_-$  (f), linear at  $0^\circ$  (c) and linear at  $45^\circ$  (e), for wavelengths of 550, 590, 630, 660 and 720 nm, also illustrated on the Poincaré sphere (d). (g) The corresponding measured spectrum (black) and the spectral resolving power (red) obtained with an SPM of  $50\ \mu\text{m}$  diameter. SPM, spectropolarimeter metasurface.

knowledge of the specific rotation's dispersion provides more detailed characterization of optically active materials, which has numerous applications in medicine, as well as the pharmaceutical and food industries.

Interleaved GPM under polychromatic illumination, which generates multiple off-axis vectorial vortex beams, enables real-time measurement of optical rotatory dispersion (ORD; see Supplementary Information). To this end, we realized a GPM consisting of four interleaved phase profiles  $\phi_g^{(1,2)}(x, y) = \sigma(k_x x \pm \varphi)$  and  $\phi_g^{(3,4)}(x, y) = \sigma(k_y y \pm 2\varphi)$ . The GPM of  $50\ \mu\text{m}$  diameter was placed between two orthogonal linear polarizers (see Materials and Methods for the experimental set-up) and vectorial vortex beams with winding numbers of 1 and 2 were obtained. When (S)- and (R)-limonene solutions were placed after the first polarizer, wavelength-dependent rotation of the fringes was observed (Figure 4b–4d). Moreover, the ORD of (S)-limonene manifested opposite behavior compared to its

enantiomer, (R)-limonene (Figure 4e and 4f), in agreement with the literature<sup>27</sup>.

Interleaved dielectric metasurface enables the implementation of a multitasking device for spectropolarimetric measurements, to instantaneously determine the polarization state of light at different wavelengths. Recently, metasurface-based polarimetry<sup>20,28</sup>, chiroptical spectroscopy<sup>29</sup> and reflective spectropolarimetry based on gap-plasmon nanoantennas<sup>4</sup> have been presented. Here we present a simple and direct spectropolarimetry approach based on a transmissive interleaved Si-based GPM. The spectropolarimeter metasurface (SPM) is composed of three interleaved phase profiles; first, a chiroptical channel of phase function  $\phi_g^{(1)} = \sigma k(x + y)$ , enabling circular dichroism spectroscopy by performing a projection of the incident wave's polarization state  $|\psi\rangle$  on the circular polarization component  $\langle \sigma | \psi \rangle$ . The projection on the linear polarization components,  $\langle L_0 | \psi \rangle$  and  $\langle L_{45} | \psi \rangle$ , is obtained by two additional binary phases  $\phi_g^{(2)}(x, y) = \sigma U_\pi(\cos(k_x x))$  and

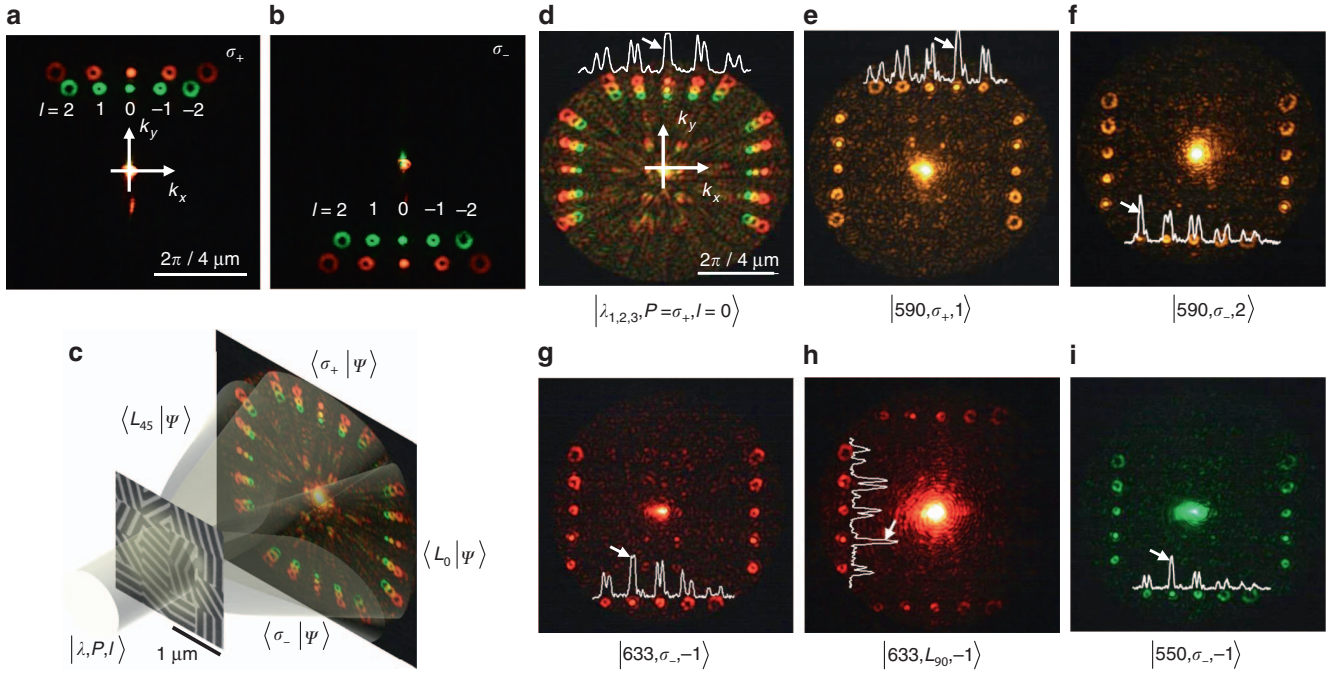


**Figure 6** Si-based OSPM. (a, b) Measured spin-flip momentum deviation of OAM harmonic wavefronts, demonstrating five off-axis spin-dependent scalar vortices at wavelengths of 550 and 670 nm;  $\sigma_{\pm}$  denotes the incident spin. (c) Schematic set-up of the OSPM of 50  $\mu\text{m}$  diameter illuminated by an arbitrarily polarized polychromatic light source. The image captured by the charge-coupled device camera was obtained for an elliptically polarized beam at  $\lambda_{1,2,3} = 550, 590$  and 633 nm with  $l = 0$ . (d–i) Measured far-field intensities for different wavelengths, polarizations and OAMs. Note,  $\lambda, P, l$  stands for the incident beam state, representing the wavelength, the polarization and the OAM, respectively.

$\phi_g^{(3)}(x, y) = \sigma U_{\pi}(\cos(k_y y)) + \sigma\pi/8$ , each providing two spatially separated diffraction orders, where  $U_{\pi}(\xi) = \{\pi, \text{ for } \xi > 0; 0 \text{ otherwise}\}$ . Note, the additional phase shift between left- and right-circular polarization ( $\sigma\pi/8$ ) rotates an incident linear polarization by  $45^\circ$ , thus facilitating the use of a single polarizer–analyzer (Figure 5a). The SPM of 50  $\mu\text{m}$  diameter was normally illuminated by a supercontinuum light source that was passed through an acousto-optic modulator and a polarization state generator. In this manner, predetermined polarization states were measured at wavelengths of 550, 590, 630, 660 and 725 nm, spanning the Stokes parameters basis ( $s_0, s_1, s_2$  and  $s_3$ ) as depicted on the Poincaré sphere (Figure 5b–5f; see Materials and Methods). Moreover, a spectral resolving power of  $\lambda/\Delta\lambda \cong 30$  was measured by taking the far-field profile (Figure 5g), in agreement with the Rayleigh criterion of the shared-aperture.

Information-carrying OAM beams may leverage optical communications and quantum information processing<sup>30</sup>, as they introduce an additional degree of freedom for increasing the capacity of free-space communications. For data transmission to capitalize on this additional degree of freedom requires the detection, characterization and sorting of the OAM optical modes. Several techniques have been suggested to measure the topological charge of a structured optical wavefront<sup>31,32</sup>. We incorporate the spectropolarimetry and OAM sensing into a GPM device that would ultimately facilitate a simultaneous detection of the frequency, polarization and OAM of light. The determination of the last parameter is achieved by the projection of an incident mode  $|l_{\text{in}}\rangle$  on a set of orthogonal OAM states  $|l_j\rangle$ , which indicates the location of the incident OAM in the set. For this purpose, we designed a shared-aperture GPM based on the harmonic response (HR) approach<sup>4</sup>. Here the HR phase function is expanded according to  $\exp(i\phi_{\text{HR}}(x)) \cong \sum_l A_l \exp[i l(kx + \varphi)]$ , resulting in a finite number of dominant

multiplexed OAM harmonic orders with identical intensities  $A_l$ , where  $lk$  is the momentum redirection of the  $l$ th order. The phase function was optimized to achieve maximal diffraction efficiency for  $-2 \leq l \leq 2$  (Ref 33). By modifying the HR function, the geometric-phase profile  $\phi_g^{(1)} = \sigma\phi_{\text{HR}}(x) + \sigma k_y y$  was obtained, generating spin-dependent dispersive OAM wavefronts possessed with circularly polarization states, ranging from  $l = -2$  to 2 (Figure 6a and 6b; see also Supplementary Fig. S4). We utilized the HR structure to achieve a multifunctional OSPM. This metasurface modifies the phase of an incident wavefront by interleaved HR phase profiles  $\phi_g^{(1)}$  and  $\phi_g^{(2)} = \sigma\phi_{\text{HR}}(y) + \sigma U_{\pi}[\cos(k_x x)]$ . Illuminating the OSPM with a plane-wave of elliptic polarization results in four symmetric sets of annular spots with a bright spot at the center, whereas those generated by  $\phi_g^{(2)}$  are transferred through linear polarizers at  $0^\circ$  and  $45^\circ$  to determine the linearly polarized components (Figure 6c; see Materials and Methods for the experimental set-up). Given an incident beam possessing an arbitrary helical phase  $\exp(i l_{\text{in}} \varphi)$ , the winding numbers of the diffracted orbital harmonics are modified by accumulating the value of the beam's topological charge  $l_{\text{in}}$ . Particularly, this modification shifts the bright spot from its original location  $l = 0$  to  $l = -l_{\text{in}}$ , enabling the determination of the incident OAM value. We demonstrate the OSPM capabilities by illuminating it with various OAM modes, which were generated by external phase modulation at different polarization states, and wavelengths (Figure 6d–6i).

## CONCLUSIONS

The shared-aperture interleaved GPM paves the way for multimodal real-time detection devices, integrated-on-chip, for multi-parameter light characterization and manipulation of light–matter interactions. The ability to encode, decode and measure the fundamental properties of light may find applications in quantum information processing,

communication and computation systems. The introduced analysis of the fundamental limitations for multiplexed phased antenna arrays can also have an impact on the design of radio frequency antenna systems.

### CONFLICT OF INTEREST

The authors declare no conflict of interest.

### ACKNOWLEDGEMENTS

This research was supported by the Israel Science Foundation (ISF), the United States—Israel Binational Science Foundation (BSF), the Israel Ministry of Science, Technology and Space, and KLA-Tencor. The fabrication was performed at the Micro-Nano Fabrication & Printing Unit (MNF&PU), Technion.

- 1 Pozar DM, Targonski SD. A shared-aperture dual-band dual-polarized microstrip array. *IEEE Trans Antennas Propag* 2001; **49**: 150–157.
- 2 Haupt RL. Interleaved thinned linear arrays. *IEEE Trans Antennas Propag* 2005; **53**: 2858–2864.
- 3 Lager IE, Trampuz C, Simeoni M, Lighthart LP. Interleaved array antennas for FMCW radar applications. *IEEE Trans Antennas Propag* 2009; **57**: 2486–2490.
- 4 Maguid E, Yulevich I, Veksler D, Kleiner V, Brongersma ML *et al*. Photonic spin-controlled multifunctional shared-aperture antenna array. *Science* 2016; **352**: 1202–1206.
- 5 Lalanpe P, Astilean S, Chavel P, Cambri E, Launois H. Blazed binary subwavelength gratings with efficiencies larger than those of conventional echelette gratings. *Opt Lett* 1998; **23**: 1081–1083.
- 6 Bomzon Z, Kleiner V, Hasman E. Pancharatnam-Berry phase in space-variant polarization-state manipulations with subwavelength gratings. *Opt Lett* 2001; **26**: 1424–1426.
- 7 Bomzon Z, Biener G, Kleiner V, Hasman E. Space-variant Pancharatnam–Berry phase optical elements with computer-generated subwavelength gratings. *Opt Lett* 2002; **27**: 1141–1143.
- 8 Yu NF, Genevet P, Kats MA, Aieta F, Tietienne JP *et al*. Light propagation with phase discontinuities: generalized laws of reflection and refraction. *Science* 2011; **334**: 333–337.
- 9 Ni XJ, Emani NK, Kildishev AV, Boltasseva A, Shalaev VM. Broadband light bending with plasmonic nanoantennas. *Science* 2012; **335**: 427.
- 10 Yin XB, Ye ZL, Rho J, Wang Y, Zhang X. Photonic spin Hall effect at metasurfaces. *Science* 2013; **339**: 1405–1407.
- 11 Pors A, Albrechtsen O, Radko IP, Bozhevolnyi SI. Gap plasmon-based metasurfaces for total control of reflected light. *Sci Rep* 2013; **3**: 2155.
- 12 Lin DM, Fan PY, Hasman E, Brongersma ML. Dielectric gradient metasurface optical elements. *Science* 2014; **345**: 298–302.
- 13 Sun JB, Wang X, Xu T, Kudyshev ZA, Cartwright AN *et al*. Spinning light on the nanoscale. *Nano Lett* 2014; **14**: 2726–2729.
- 14 Chong KE, Staude I, James A, Dominguez J, Liu S *et al*. Polarization-independent Silicon metadevices for efficient optical wavefront control. *Nano Lett* 2015; **15**: 5369–5374.

- 15 Zeng JW, Gao J, Luk TS, Litchinitser NM, Yang XD. Structuring light by concentric-ring patterned magnetic metamaterial cavities. *Nano Lett* 2015; **15**: 5363–5368.
- 16 Arbabi A, Horie Y, Bagheri M, Faraon A. Dielectric metasurfaces for complete control of phase and polarization with subwavelength spatial resolution and high transmission. *Nat Nanotechnol* 2015; **10**: 937–943.
- 17 Zheng GX, Mühlenbernd H, Kenney M, Li GX, Zentgraf T *et al*. Metasurface holograms reaching 80% efficiency. *Nat Nanotechnol* 2015; **10**: 308–312.
- 18 Berry MV. The adiabatic phase and Pancharatnam's phase for polarized light. *J Mod Opt* 1987; **34**: 1401–1407.
- 19 Bliokh KY, Rodríguez-Fortuño FJ, Nori F, Zayats AV. Spin-orbit interactions of light. *Nat Photonics* 2015; **9**: 796–808.
- 20 Gorodetski Y, Biener G, Niv A, Kleiner V, Hasman E. Space-variant polarization manipulation for far-field polarimetry by use of subwavelength dielectric gratings. *Opt Lett* 2005; **30**: 2245–2247.
- 21 Hillery M, O'Connell RF, Scully MO, Wigner EP. Distribution functions in physics: fundamentals. *Phys Rep* 1984; **106**: 121–167.
- 22 Parrondo JMR, Horowitz JM, Sagawa T. Thermodynamics of information. *Nat Phys* 2015; **11**: 131–139.
- 23 Shannon CE. A mathematical theory of communication. *Bell Syst Tech J* 1948; **27**: 379–423.
- 24 Cover TM, Thomas JA *Elements of Information Theory*. New Jersey: Wiley; 2006.
- 25 Shvedov V, Davoya AR, Hnatovsky C, Engheta N, Krolkowski W. A long-range polarization-controlled optical tractor beam. *Nat Photon* 2014; **8**: 846–850.
- 26 Miao P, Zhang Z, Sun J, Walasik W, Longhi S *et al*. Orbital angular momentum microlaser. *Science* 2016; **353**: 464–467.
- 27 Fujiki M, Jalilah AJ, Suzuki N, Taguchi M, Zhang W *et al*. Chiral optofluidics: gigantic circularly polarized light enhancement of all-trans-poly(9,9-di-n-octylfluorene-2,7-vinylene) during mirror-symmetry-breaking aggregation by optically tuning fluidic media. *RSC Adv* 2012; **2**: 6663–6671.
- 28 Pors A, Nielsen MG, Bozhevolnyi SI. Plasmonic metagratings for simultaneous determination of Stokes parameters. *Optica* 2015; **2**: 716–723.
- 29 Shaltout A, Liu JJ, Kildishev A, Shalaev V. Photonic spin Hall effect in gap-plasmon metasurfaces for on-chip chiroptical spectroscopy. *Optica* 2015; **2**: 860–863.
- 30 Wang J, Yang JY, Fazal IM, Ahmed N, Yan Y *et al*. Terabit free-space data transmission employing orbital angular momentum multiplexing. *Nat Photon* 2012; **6**: 488–496.
- 31 Berkhout GCG, Lavery MPJ, Courtial J, Beijersbergen MW, Padgett MJ. Efficient sorting of orbital angular momentum states of light. *Phys Rev Lett* 2010; **105**: 153601.
- 32 Mirhosseini M, Malik M, Shi ZM, Boyd RW. Efficient separation of the orbital angular momentum eigenstates of light. *Nat Commun* 2013; **4**: 2781.
- 33 Dammann H, Görtler K. High-efficiency in-line multiple imaging by means of multiple phase holograms. *Opt Commun* 1971; **3**: 312–315.



This work is licensed under a Creative Commons Attribution-NonCommercial-NoDerivs 4.0 International License. The images or other third party material in this article are included in the article's Creative Commons license, unless indicated otherwise in the credit line; if the material is not included under the Creative Commons license, users will need to obtain permission from the license holder to reproduce the material. To view a copy of this license, visit <http://creativecommons.org/licenses/by-nc-nd/4.0/>

© The Author(s) 2017

Supplementary Information for this article can be found on the *Light: Science & Applications*' website (<http://www.nature.com/lsa>).